

Virtual histology of an entire mouse brain from formalin fixation to paraffin embedding. Part 2: Volumetric strain fields and local contrast changes

Griffin Rodgers^{a,b}, Christine Tanner^{a,b,*}, Georg Schulz^{a,b}, Alexandra Migga^{a,b}, Willy Kuo^{c,d}, Christos Bikis^{a,b,e}, Mario Scheel^f, Vartan Kurtcuoglu^{c,d}, Timm Weitkamp^f, Bert Müller^{a,b}

^a Biomaterials Science Center, Department of Biomedical Engineering, University of Basel, 4123 Allschwil, Switzerland

^b Biomaterials Science Center, Department of Clinical Research, University Hospital Basel, 4031 Basel, Switzerland

^c The Interface Group, Institute of Physiology, University of Zurich, 8057 Zurich, Switzerland

^d National Centre of Competence in Research, Kidney.CH, 8057 Zurich, Switzerland

^e Integrierte Psychiatrie Winterthur – Zürcher Unterland, 8408 Winterthur, Switzerland

^f Synchrotron Soleil, 91192 Gif-sur-Yvette, France

ARTICLE INFO

Keywords:

Synchrotron radiation-based microtomography
Neuroimaging
Non-rigid registration
Non-uniform shrinkage
Embedding media for contrast enhancement in brain tissue

ABSTRACT

Background: Fixation and embedding of *post mortem* brain tissue is a pre-requisite for both gold-standard conventional histology and X-ray virtual histology. This process alters the morphology and density of the brain microanatomy.

New method: To quantify these changes, we employed synchrotron radiation-based hard X-ray tomography with 3 μm voxel length to visualize the same mouse brain after fixation in 4% formalin, immersion in ethanol solutions (50%, 70%, 80%, 90%, and 100%), xylene, and finally after embedding in a paraffin block. The volumetric data were non-rigidly registered to the initial formalin-fixed state to align the microanatomy within the entire mouse brain.

Results: Volumetric strain fields were used to characterize local shrinkage, which was found to depend on the anatomical region and distance to external surface. X-ray contrast was altered and enhanced by preparation-induced inter-tissue density changes. The preparation step can be selected to highlight specific anatomical features. For example, fiber tract contrast is amplified in 100% ethanol.

Comparison with existing methods: Our method provides volumetric strain fields, unlike approaches based on feature-to-feature or volume measurements. Volumetric strain fields are produced by non-rigid registration, which is less labor-intensive and observer-dependent than volume change measurements based on manual segmentations. X-ray microtomography provides spatial resolution at least an order of magnitude higher than magnetic resonance microscopy, allowing for analysis of morphology and density changes within the brain's microanatomy.

Conclusion: Our approach belongs to three-dimensional virtual histology with isotropic micrometer spatial resolution and therefore complements atlases based on a combination of magnetic resonance microscopy and optical micrographs of serial histological sections.

1. Introduction

Histology is the gold standard for investigations of brain microanatomy, as it provides sub-micron resolution in two dimensions with a variety of functional stains (Culling, 1974). Virtual histology based on hard X-ray microtomography (Albers et al., 2018) is an emerging complementary technique that can reveal the brain's cytoarchitecture in three dimensions (Dyer et al., 2017; Hieber et al., 2016; Khimchenko

et al., 2016; Töpperwien et al., 2018, 2020) with isotropic spatial resolution down to and even below the optical limit (Khimchenko et al., 2018; Kuan et al., 2020).

Tissue fixation and embedding are prerequisites for *post mortem* neuroimaging with both conventional and virtual histology. During the standard histological preparation (Culling, 1974), the exchange of formalin with alcohol, alcohol with xylene, and xylene with paraffin alters the densities of physically soft tissues and thereby changes the

* Corresponding author at: Biomaterials Science Center, Department of Biomedical Engineering, University of Basel, 4123 Allschwil, Switzerland.

E-mail address: christine.tanner@unibas.ch (C. Tanner).

<https://doi.org/10.1016/j.jneumeth.2021.109385>

Received 15 July 2021; Accepted 7 October 2021

Available online 9 October 2021

0165-0270/© 2021 The Authors. Published by Elsevier B.V. This is an open access article under the CC BY license (<http://creativecommons.org/licenses/by/4.0/>).

local X-ray absorption coefficient. Neurons, for example, show significant X-ray contrast enhancement from paraffin embedding (Töpperwien et al., 2019). In this sense, sample embedding can be thought of analogously to staining (Müller et al., 2008) and should be considered as an experimental parameter to be optimized (Töpperwien et al., 2019; Strotton et al., 2018). An understanding of tissue density and X-ray contrast changes for the whole brain is therefore desirable, as it would facilitate the selection of embedding state for the visualization of each anatomical structure.

In addition to density changes, paraffin embedding introduces non-uniform shrinkage. Though this has been studied for over a century (Hardy, 1899), until now most studies quantifying shrinkage are based on total volume change or length measurements of tissue sections (Quester and Schröder, 1997). To map shrinkage in three dimensions, a non-destructive volumetric imaging modality is needed. For example, strain fields in the human brain were tracked after extraction from the skull and during formalin fixation with magnetic resonance imaging (MRI) (Schulz et al., 2011). MRI was also used to quantify volume changes of segmented anatomical regions from the *in vivo* state to the formalin fixed state (Ma et al., 2008). Unfortunately, MRI contrast is weak after dehydration for paraffin embedding (Wehrl et al., 2015). Total volume and landmark positions were tracked in MR and computed tomography images to assess shrinkage of the mouse brain with various fixatives (Wehrl et al., 2015). However, all of the above studies lack spatial and density resolution to differentiate effects within smaller anatomical regions.

The objective of this two-part study is to combine isotropic micrometer-resolution imaging with non-rigid registration to quantify morphological and density changes as a result of tissue embedding. To this end, we employ synchrotron radiation-based X-ray micro computed tomography to visualize an entire mouse brain over the course of paraffin embedding, i.e. in formalin, five ascending ethanol solutions (50%, 70%, 80%, 90%, and 100%), xylene, and paraffin. We aim to measure global and local volume change, determine the best embedding medium for visualization of selected anatomical features, and uncover the basis for the dramatic X-ray contrast enhancement observed in embedded tissues.

The first part of this investigation (Rodgers et al., 2021a) reports the brain preparation and paraffin embedding protocol, acquisition and reconstruction of the tomography data from laboratory- and synchrotron radiation-based microtomography, and analysis of volume and density changes of the full brain and segmented anatomical features. Part 2 complements that study by addressing the non-rigid registration of the tomography data, its validation, and the analysis of volumetric strain fields and local contrast changes.

2. Materials and methods

2.1. Sample preparation and data acquisition

A detailed description of the sample preparation, image acquisition, and tomographic reconstruction is presented in Part 1 (Rodgers et al., 2021a).

2.2. Non-rigid registration

The open-source software toolbox *elastix* (Klein et al., 2010; Shamonin et al., 2014) (version 4.9) was used for registration of the tomography data. Registrations were performed on a workstation with an Intel® Xeon® CPU (E5-2637 v2 3.50 GHz) and 144 GB memory. The dataset of the formalin-fixed brain was selected as the reference dataset for all registrations. The non-rigid registration pipeline consisted of three steps: (1) coarse manual affine pre-alignment, (2) automatic multi-resolution affine registration, and (3) automatic multi-resolution B-spline registration. A final rigid transformation (4) was used for displaying the data in anatomical planes.

Step (1) facilitates the automatic registrations by starting from a reasonable alignment. Using the open-source software *ITK-SNAP* (Yushkevich et al., 2006) (version 3.8.0) and the downsampled datasets, three rotation angles, three translations, and one scaling factor were selected for a coarse alignment. Determining these parameters took about one minute per dataset.

The registrations in steps (2) and (3) relied on the $3 \times$ binned datasets to speed up registration, as the data size of the unbinned reconstructed volumes ranged from 210 to 260 GB for single precision (32-bit depth). Textures and edges were enhanced with a standard deviation filter with $3 \times 3 \times 3$ voxel neighborhood. Background pixels were excluded from the registration optimization to avoid influence of the surrounding medium and sample holder. This was achieved by means of coarse masks created by simple semi-automatic segmentation of the full brain *via* thresholding, morphological closing, and largest connected structure extraction. Mattes mutual information was selected as the similarity measure to account for non-linear intensity changes due to the selected embedding materials. Optimization was based on stochastic gradient descent. The registration parameter files are freely available (Rodgers et al., 2021c).

For step (2), affine registration was done with four resolutions (smoothing and downsampling), 1,000 iterations per resolution, and 65,536 random spatial samples. The number of spatial samples was selected as a compromise between registration speed and fluctuations in the similarity measure due to sample variations. Affine registration of each dataset took around 35 min.

For step (3), non-rigid registration was based on a B-Spline transform, where the displacements at a grid of control points are interpolated by cubic B-Splines. The degrees of freedom are controlled by the grid spacing. We selected a spacing of $12 \times 12 \times 12$ voxels as this choice was the finest grid spacing that allowed the full volume registration to run on a single workstation with 144 GB of RAM and showed sufficient flexibility in initial tests. This approach corresponds to nearly 7 million degrees of freedom. To avoid unrealistic deformations in homogeneous regions, a bending energy term was added to the cost function. The weighting of this regularization term was optimized by plotting the image dissimilarity versus the bending energy after registrations with various grid spacings and weights (Rodgers et al., 2021b). A weight was then chosen which was on the Pareto front and close to the elbow of the resulting L-shape curve (Rodgers et al., 2021b; Hansen, 2000). Five resolutions (smoothing without downsampling) were used with 2,000 iterations each and 131,072 random spatial samples. This registration took around 7.5 h per dataset.

After step (3), all datasets were in the coordinate frame of the formalin dataset. Step (4) applied a rigid transformation to all datasets for display in a desired coordinate frame, i.e. sagittal, axial, and coronal planes. This single transformation was manually determined in *ITK-SNAP* in around one minute.

The datasets were warped only once with the composition of transformations produced in steps (1)-(4). We note that this transformation can be applied to any volume in the same coordinate frame as the floating dataset, for example if an alternative filtering option such as phase retrieval is more desirable for visualization or subsequent analysis. Resampling was done with linear interpolation to avoid over-shoots where edge enhancement is observed. The warping took about 20 min for the $3 \times 3 \times 3$ binned datasets. The entire unbinned dataset could not be warped due to memory limitations, therefore regions of interest were individually warped by applying the transformation from registration of the $3 \times 3 \times 3$ binned dataset.

The voxel-wise volume change as the result of the registrations was calculated from the determinant of the Jacobian of the transformation. The program *transformix* (Klein et al., 2010; Shamonin et al., 2014) (version 4.9) was used to calculate these values for the composition of transformations given from steps (1)-(4). These transformations have been made publicly available along with the $3 \times 3 \times 3$ datasets used for registration (Rodgers et al., 2021c).

2.3. Evaluation of registration accuracy

Validation of non-rigid registration is challenging as the ground truth is unknown and difficult to manually establish (Crum et al., 2003; Schnabel et al., 2003; Plum et al., 2016). Here, the registration accuracy was qualitatively assessed with visual inspection. Quantitative assessment was based on the Dice Similarity Coefficient (Dice, 1945), median surface-to-surface distance, and volume change error of segmentations of the full brain and ventricles. These structures could be confidently segmented thanks to the contrast between tissue and the embedding material. The metrics were calculated between the reference (formalin) and the transformed segmentations (100% ethanol, xylene, and paraffin).

Consider the reference segmentation S_{ref} , the floating segmentation S_{flo} , and the floating segmentation transformed to the reference space $T(S_{\text{flo}})$ via the transformation T found by registration. The Dice similarity coefficient was defined as

$$DSC = 2|S_{\text{ref}} \cap T(S_{\text{flo}})| / (|S_{\text{ref}}| + |T(S_{\text{flo}})|).$$

The median surface-to-surface distance was defined as

$$d_{\text{med}} = \text{median}\{\mathcal{S}(S_{\text{ref}}, T(S_{\text{flo}})) \cup \mathcal{S}(T(S_{\text{flo}}), S_{\text{ref}})\},$$

where $\mathcal{S}(S_{\text{ref}}, T(S_{\text{flo}}))$ is the set of the shortest distances from all surface points of S_{ref} to the surface of $T(S_{\text{flo}})$. The volume change error was calculated by

$$E_{\text{rV}} = rV_{\text{reg}} / rV_{\text{seg}} - 1.$$

Here $rV_{\text{reg}} = V(S_{\text{flo}}) / V(T(S_{\text{flo}}))$ is the volume change ratio using the transformed floating segmentation and $rV_{\text{seg}} = V(S_{\text{flo}}) / V(S_{\text{ref}})$ is the volume change ratio using the reference segmentation.

Dice overlap scores are known to overstate registration quality for large volume segmentations because surface differences have small contributions. Hence, we included median surface-to-surface distances, which are entirely surface-based with the median providing robustness to local segmentation differences. Volume change error was included, as it characterizes the difference between volume change as measured by segmentation vs. registration. For reference, a Dice score of unity indicates perfect overlap and zero indicates no overlap. A surface-to-surface distance of zero indicates precise alignment and large values indicate poor alignment. A volume change error of 0% (+100%) indicates that the volume change measured by registration matches (is two

times larger than) the volume change measured by segmentation.

2.4. Quality assurance for data processing pipeline

We identified the following sources of artefacts or losses of data quality during registration (Section 2.2): overfitting, folding, under- or over-regularization (e.g. wavy or stiff edges). To reduce the risk of these artefacts, orthogonal slices of all datasets were visually inspected after each processing step. For consistency, parameters were selected only if they allowed for acceptable performance on all datasets. We analyzed L-curves to support parameter selection to reduce over- or under-regularization during registration (Rodgers et al., 2021b).

3. Results

3.1. Quality of non-rigid registration

Registration results were visually evaluated within the formalin-fixed and 100% ethanol immersed brain datasets in Figs. 1 and 2. Fig. 1 shows representative virtual axial slices of the reference formalin-fixed dataset (Fig. 1R), the original floating dataset (Fig. 1F), the manually rigid pre-aligned dataset (Fig. 1S1), the automatically affine registered dataset (Fig. 1S2), and the automatically B-spline registered dataset (Fig. 1S3). These selected virtual slices show the steps of registration described in Section 2.2.

The affine registration was characterized by twelve degrees of freedom (three translation, three rotation, three scaling, and three skew parameters) with the same geometric transformation for all voxels and thus a uniform volume change. It resulted in a coarse alignment of the full brain (Fig. 1S2) with many internal features not matching (cf. Fig. 2). The B-spline transform used here contained nearly 7 million degrees of freedom and thus improved on the affine registration with local deformations to match fine structures. This improvement became apparent upon closer visual inspection as depicted for three examples in Fig. 2.

Fig. 2 shows magnified views of the regions of interest highlighted by the dashed yellow squares in Fig. 1R. Overlays are shown to visually compare the performance of automatic affine and automatic B-spline registrations. The B-spline registration showed excellent results within most of the brain, even accurately aligning individual cells (see the hippocampus, top arrow of middle row). Discrepancies were found in regions where large local deformations occurred, e.g. within the

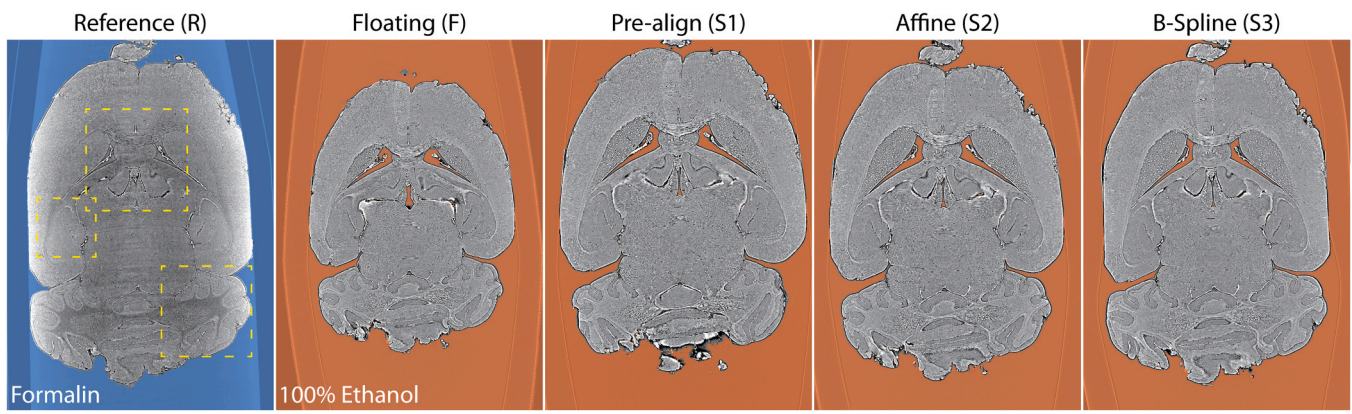


Fig. 1. Registration results. Floating datasets (F, here 100% ethanol) were registered to the reference formalin-fixed dataset (R) via a manual pre-alignment (S1) followed by automatic affine (S2) and then automatic B-spline registration (S3). Affine registration allows for global translation, rotation, scaling, and shearing (12 degrees of freedom), while B-spline allows for local deformations based on displacements of a grid of control points (in this work, about 7 million degrees of freedom were used). A bending energy regularization term was imposed on the B-spline registration to penalize large local deformations. The registration was optimized within full brain masks (shown without color) to avoid influence of the surrounding medium and the sample holder. The yellow dashed boxes show regions of interest for detailed comparison in Fig. 2. The scale bar is 3 mm and the grayscale range is given by mean \pm 2 standard deviations of the intensities in the full brain mask per embedding.

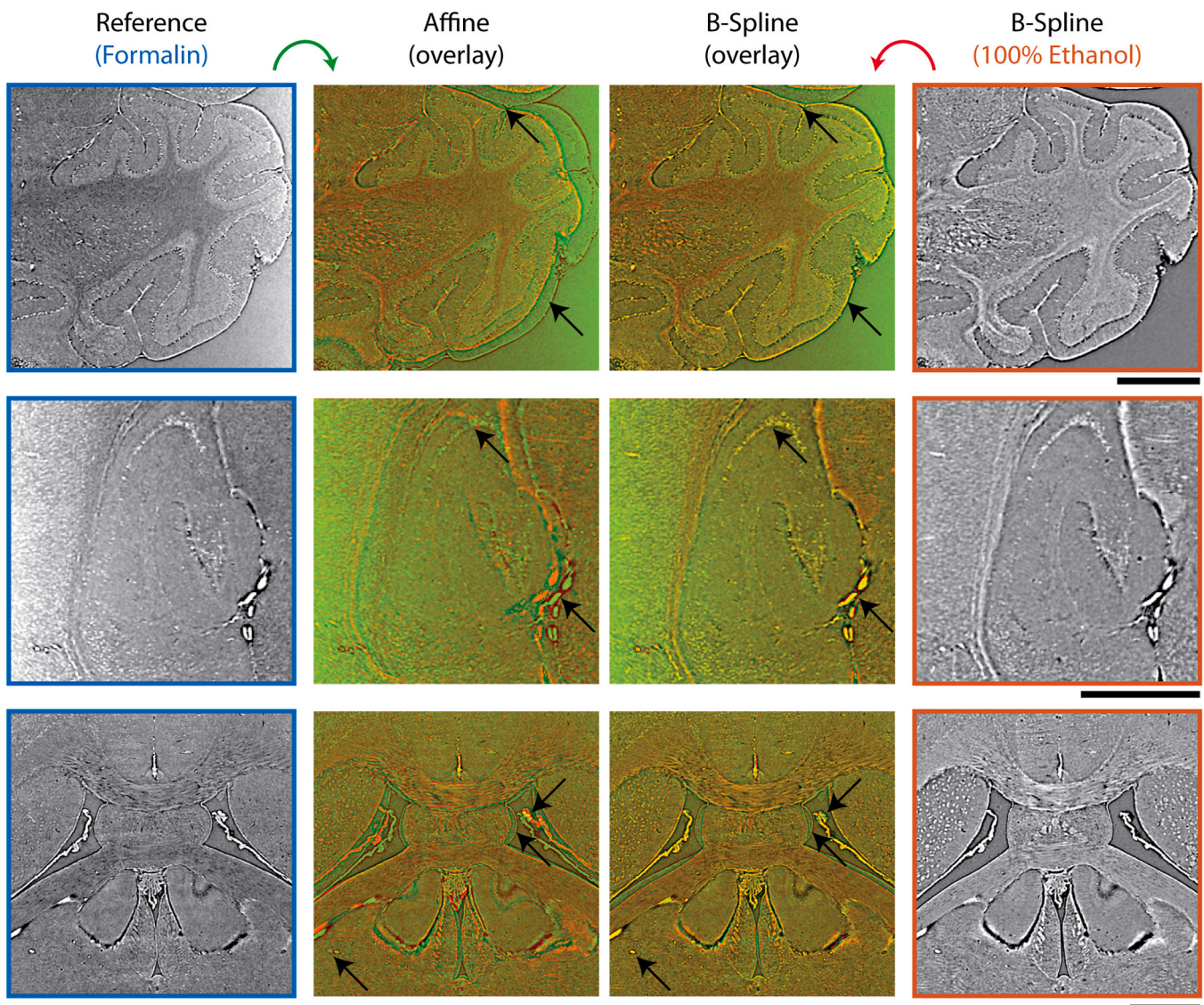


Fig. 2. Comparing affine and non-rigid (B-spline) registration. The three regions of interest marked in Fig. 1 are shown in the reference formalin (column 1) and the B-spline registered 100% ethanol (column 4) datasets. Alignment performance of affine (column 2) and B-spline registrations (column 3) are shown with overlays, green: formalin, red: 100% ethanol. The outer borders of the cerebellum (top) were matched by B-spline (bottom arrow) with the exception of regions of complete collapse or expansion (top arrow); (middle) matching of fine structures near the hippocampus indicates excellent agreement for the B-spline (both arrows); (bottom) the ventricle walls (middle arrow) presented a challenge due to strong local deformations, but nearby regions showed excellent agreement, see e.g. the plexus choroideus (top arrow) or the vessel in the lower left (bottom arrow). All scale bars correspond to 1 mm and the grayscale range is given by mean \pm 2 standard deviations of the intensities in the full brain mask per embedding.

ventricles (bottom row, top arrow), as well as at locations of complete expansion or collapse, e.g. at the border between the cerebellum and cerebral cortex (top row, top arrow).

The registration accuracy was also assessed with Dice overlap, median surface-to-surface distances, and volume difference, see Table 1. Note that the metrics were evaluated on the $3\times$ binned datasets with pixel length of $9.3\ \mu\text{m}$, as this binning factor was used for registration. All metrics showed a substantial registration improvement from affine to B-spline approaches.

3.2. Mapping the local volumetric strain

The determinant of the spatial Jacobian of the transformation found during registration gives the volume change ratio (corresponding to the floating volume divided by reference volume, i.e. $V(I_{\text{flo}}(x))/V(I_{\text{ref}}(x))$) for each voxel in the dataset. Note that the transformation is the composition of all steps (pre-align, affine and non-rigid). Volumetric

Table 1

Registration quality metrics. Segmentations of the full brain and ventricles were used to assess registration accuracy. Dice similarity coefficient, median surface-to-surface distance, and the volume change error were calculated between the reference (formalin) and the transformed segmentations (100% ethanol, xylene, and paraffin).

	Dice Similarity Coefficient		Surface-to-surface distance [μm]		Volume change error	
	Affine	B-spline	Affine	B-spline	Affine	B-spline
Full brain						
100% ethanol	0.953	0.975	47.3	13.1	-3.2%	-1.9%
xylene	0.935	0.974	80.0	11.2	-9.7%	-1.2%
paraffin	0.890	0.951	142.7	46.4	-22.6%	-8.5%
Ventricles						
100% ethanol	0.503	0.677	20.7	9.3	-50.2%	-31.7%
xylene	0.507	0.655	26.2	9.3	-33.0%	-10.3%
paraffin	0.440	0.592	20.7	9.3	-50.4%	-33.5%

strain fields (volume change ratio minus 1, given as percentages in the Figs. 3 and 7) show the local compression or expansion from the reference (formalin) to the floating dataset. Fig. 3 shows renderings of the 100% ethanol, xylene, and paraffin datasets before and after non-rigid registration, slices through the volumetric strain fields, and histograms of the voxel-wise volumetric strains for the entire dataset of each preparation step.

Fig. 3 (left) illustrates the volumetric strain fields for the main steps, namely 100% ethanol, xylene, and paraffin. All embedding steps showed a similar pattern of volume change: greater volume change was observed towards the brain's outer surface, e.g. in the cerebral cortex, while less shrinkage was found in the region around the ventricles. Volume change appeared to be related to both distance from the embedding medium and anatomical region. For example, the thalamus could be identified from the volumetric strain fields by its smaller volume change. Similarly, white matter, granular, and molecular layers of the cerebellum could be seen from interfaces in the strain field maps. The histograms on the right side of Fig. 3 display the distribution of voxel-wise volumetric strain within the brain. Increasing shrinkage was seen over the course of embedding: for 50%, 70%, 80%, 90%, 100% ethanol, xylene, and paraffin, the median volumetric strain (interquartile range) from formalin to these steps was -5% (10%), -12% (16%), -23% (18%), -37% (13%), -39% (11%), -41% (12%), and -56% (10%).

3.3. Local X-ray absorption of corresponding features

Registration allows for side-by-side comparisons of the X-ray contrast in corresponding anatomical regions. Fig. 4 shows a sagittal slice (1) through the registered $3\times$ binned datasets in formalin (A), 100% ethanol (B), xylene (C), and paraffin (D). The cerebellum (2), hippocampus (3), and caudoputamen (4) are highlighted with zoom-ins. The difference in absorption coefficient μ between the brain and surrounding medium became larger with each subsequent step.

Fig. 5 shows magnified views of the aligned unbinned datasets with pixel size $3.1\ \mu\text{m}$. These zooms are within the regions of interest of the sagittal slices from Fig. 4 A1. For all datasets, spatial and density resolution were sufficient to identify individual cells. At this resolution, local density changes determined which features can be easily distinguished. The increased relative density of white matter in ethanol made identification of the extent of the granular layer difficult (B1). The same border was clearly distinguishable in xylene and paraffin (C1 & D1). The border between caudoputamen and the fiber tracks was clearest in 100% ethanol (B2) and nearly invisible in paraffin (D2).

Fig. 6 demonstrates the effect of ascending ethanol solutions on the fiber tract contrast. Regions of interest in coronal, axial, and sagittal virtual slices are shown in all steps of the $3\times$ binned datasets. A notable feature in the formalin-fixed brain is the white matter and other fiber tracts, which had μ below that of the surrounding brain tissue (see also e.g. Fig. 4A2). Contrast between fiber tracts and the surrounding tissue increased with ethanol concentration. The visibility of fibers was reduced in xylene and nearly zero when embedded in paraffin.

4. Discussion

The combination of slicing-free three-dimensional imaging and non-rigid registration allowed for the generation of volumetric strain fields and side-by-side comparison of tissue density in the selected preparation stages. As it can be applied after brain extraction and immediately prior to histological sectioning, X-ray virtual histology can also be incorporated into the creation of brain atlases. This procedure can be applied to other tissue types and preparation protocols to measure non-uniform volume changes and to select an optimized preparation with respect to X-ray contrast.

We analyzed brain shrinkage during the embedding protocol with two methods: manual segmentation of anatomical features (Rodgers,

2021a) and non-rigid registration (described in this Part 2). The approach based on non-rigid registration generates volumetric strain fields for the entire brain without the need for time-consuming manual segmentation. This offers a visual scheme that is more intuitive than tabulated volume measurements. For example, the maps shown in Fig. 3 allow for quick determination of the effect of tissue preparation on any anatomical region. Overlaying the anatomical information of the tomographic data with these strain fields (e.g. in Fig. 7 column 2) allows for studying volume changes within a given region in three dimensions.

A challenge of the non-rigid registration approach is that volumetric strain fields depend on the transformation model used for registration, with highly regularized models leading to smooth strain fields (Rodgers et al., 2021b). We tuned registration parameters for one dataset (xylene) and applied them to the other embedding states. The metrics in Table 1 and visual inspection of the registered datasets indicated that registration parameters were not over-tuned. We expect that parameter tuning for each embedding state, e.g. with the L-curve method (Rodgers et al., 2021b), may provide better registration accuracy and more realistic strain fields, as the contrast changes affect the image similarity metric and thus influence the regularization weight. For population studies, we do not expect that tuning parameters for each mouse will be necessary as long as the identical experimental setup and imaging parameters are used. The current model was optimized for the $3\times$ binned volumes, i.e. for an isotropic voxel length of about $10\ \mu\text{m}$. Registration of the unbinned data would be more computationally demanding but allow for alignment of microstructures with smaller size and/or for the determination of more detailed volumetric strain fields. In this study, such a registration would have exceeded the available memory. A framework should be developed for *elastix* registration of sub-volumes with a large number of degrees of freedom without exceeding standard workstation resources.

Nevertheless, the calculated volumetric strain fields revealed that the shrinkage from the formalin-fixed state to each of the preparation steps was a function of both anatomical region and distance to the brain surface (Fig. 3). This distance dependence suggests shrinkage is related to diffusion of the embedding material into the brain tissue. Fig. 7 compares the volumetric strain field of the paraffin embedded brain with a three-dimensional distance transform of the segmentation of the full brain in paraffin. An overlay of the volumetric strain fields on the tomographic data reveals the dependence on anatomical region. The distance transform shows a first approximation of equal diffusion coefficient for all brain tissue. Deviation of the shrinkage maps from the distance transform is due to tissue composition-dependent uptake of embedding material, altered diffusion across anatomical borders, and decreased access of embedding media through smaller channels such as the ventricles.

Due to the role of diffusion, we expect geometry-dependent volumetric strain fields during preparation of smaller tissue sections such as biopsies (Katsamenis et al., 2019) and punches (Hieber et al., 2016; Töpferwien et al., 2018, 2019). The methodology presented here, or a more accessible variation based on laboratory X-ray microtomography, could be easily adapted to quantify and correct preparation-based tissue deformations.

In this experiment, the choice of embedding material did not alter the spatial resolution of the measurement setup. The data of the paraffin-embedded brain appears to have lower spatial resolution in Fig. 5 because it has been interpolated to be displayed as registered to formalin-fixed brain. Due to shrinkage, a higher spatial resolution may be desirable for studying samples embedded in paraffin compared to samples fixed in formalin. This is in contrast to the concept of expansion microscopy, where a sample is deliberately swollen to increase spatial resolution (Chen et al., 2015).

Individual cells were near the resolution limit of this study and therefore cellular shrinkage could not be accurately characterized. Töpferwien and co-workers performed sub-micrometer virtual histology of 1 mm diameter punches from the cerebellum of formalin-fixed,

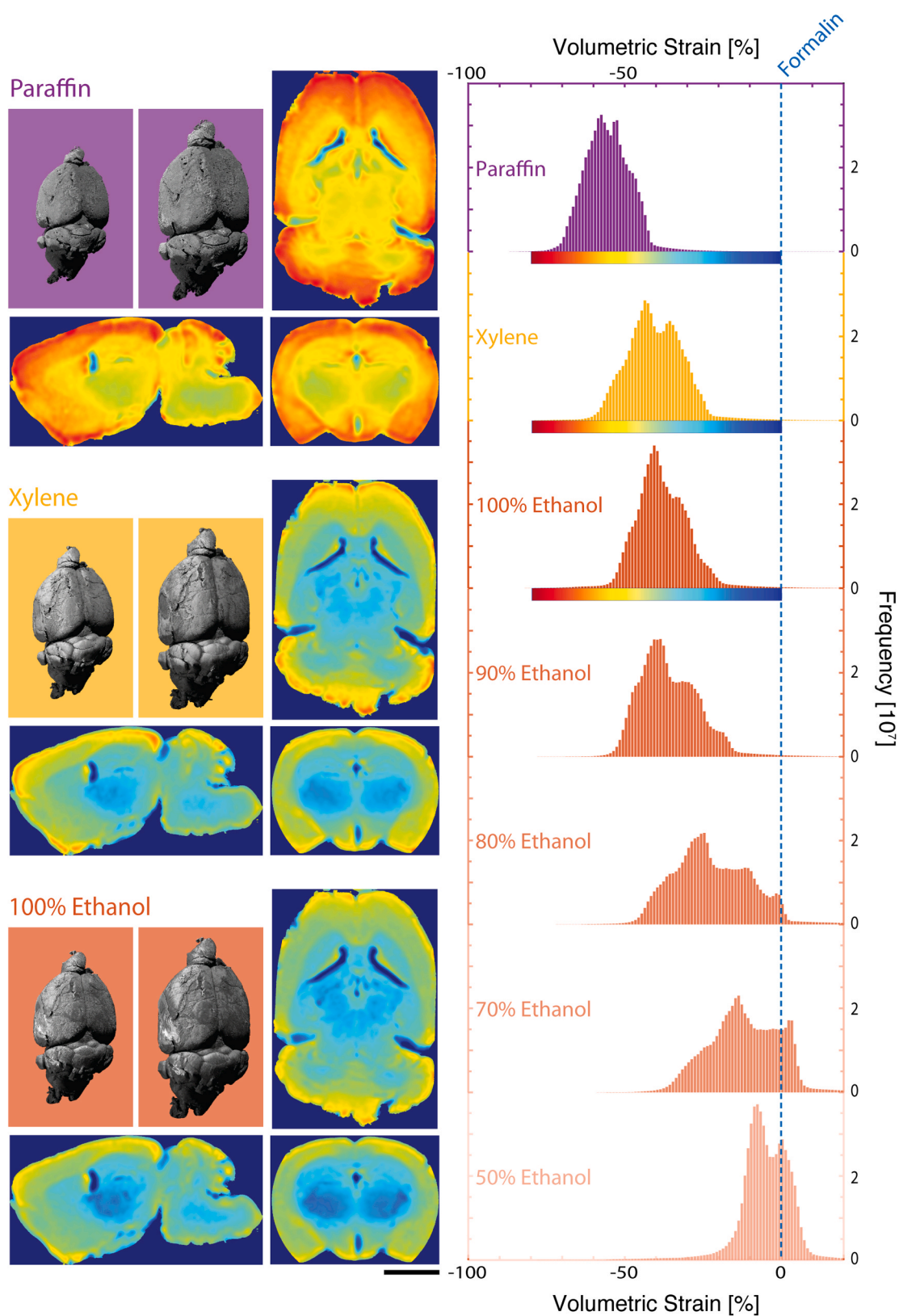


Fig. 3. Volumetric strain fields from mouse brain embedding. Non-rigid registration allows for extraction of the volume change of each voxel in the dataset. The left column shows a volume rendering of the brain before and after registration as well as the associated volumetric strain fields on selected sagittal, coronal, and axial slices (scale bar 3 mm). The highest volume shrinkage was observed towards the outer edges of the brain, e.g. in the cerebral cortex. The region around the ventricles showed the least shrinkage. Volumetric strain appeared to be related to both distance from the embedding medium and anatomical region. Histograms of the volumetric strain fields are given in the right column for all embedding steps. A voxel volume strain of zero corresponds to no volume change from formalin.

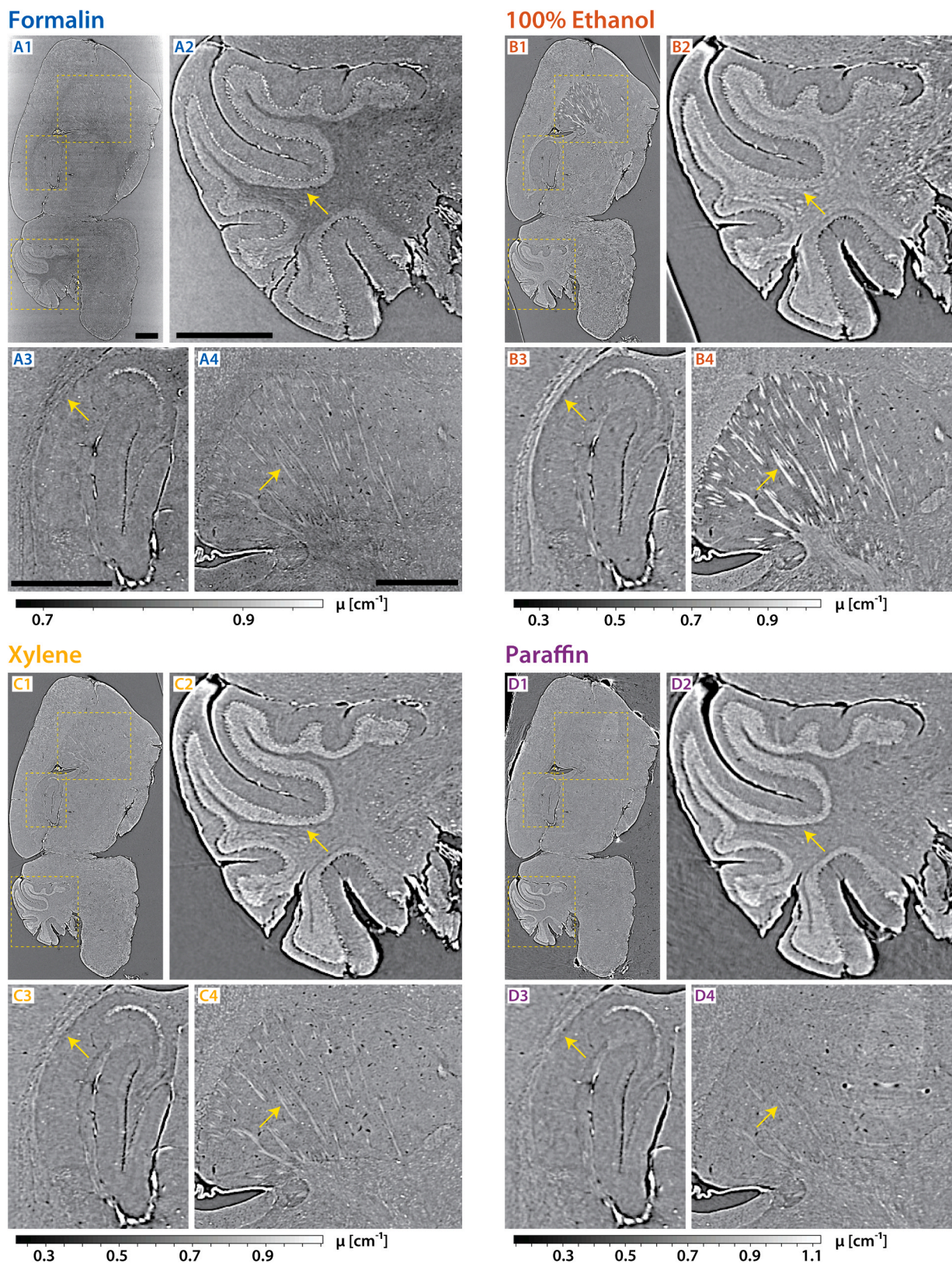


Fig. 4. Direct comparison of tissue density and contrast over the course of embedding: $3\times$ -binned datasets in formalin (A), 100% ethanol (B), xylene (C), and paraffin (D). Corresponding sagittal slices of the registered datasets (A1-D1) indicate regions of interest in the cerebellum (A2-D2), hippocampus (A3-D3), and caudoputamen (A4-D4). In the cerebellum (A2-D2), the relative densities of white matter and granular layer changed dramatically, see arrow. The hippocampus (A3-D3) showed similar contrast throughout embedding, though the nearby fiber tracts became more dense in 100% ethanol (arrow, B3). The fiber tracts in the caudoputamen (A4-D4) were clearly visible in ethanol (B4) and barely visible in paraffin (D4, arrow). All scale bars are 1 mm and the grayscale range is given by mean \pm 2 standard deviations of the intensities in the full brain mask per embedding.

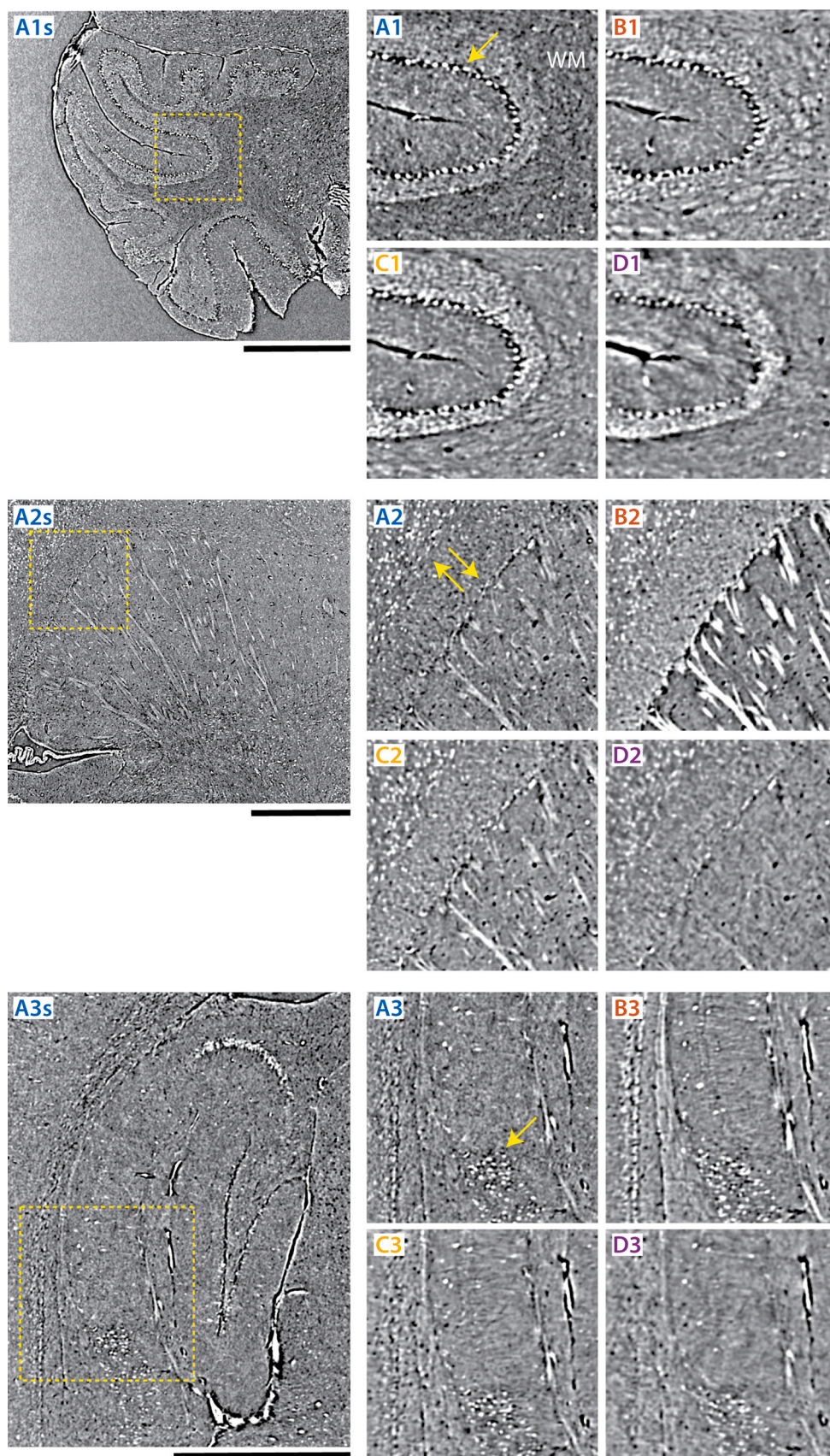
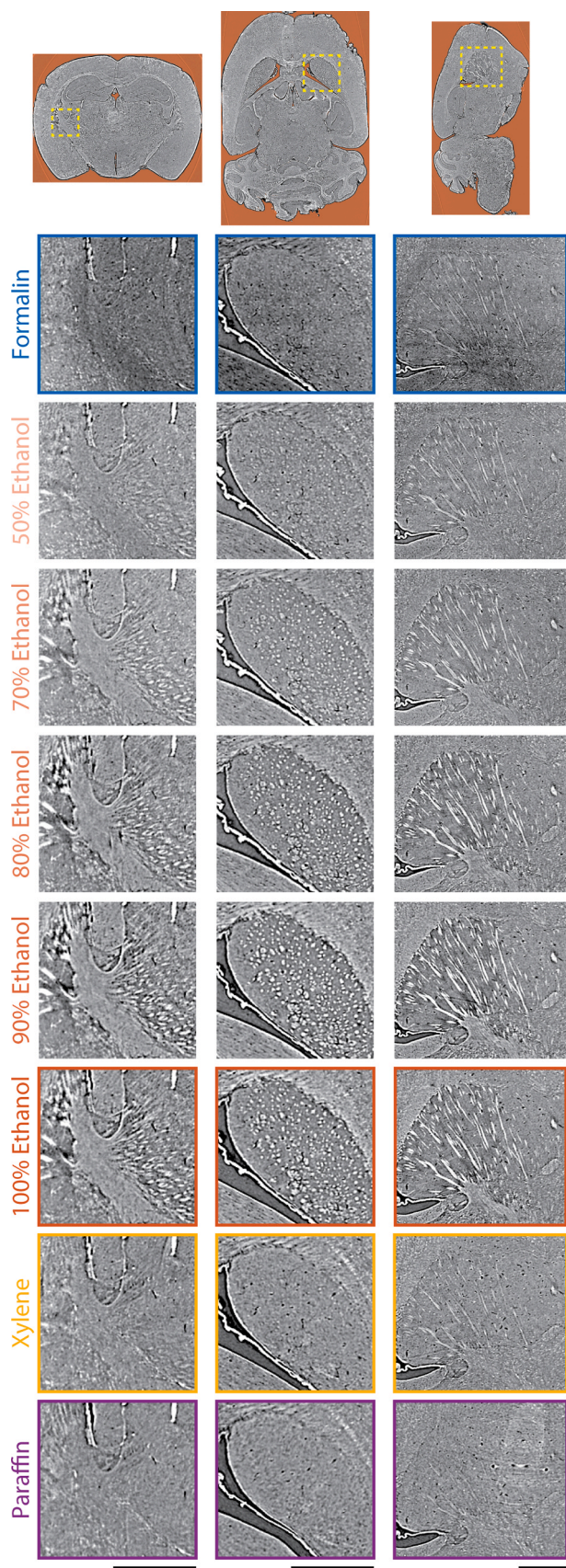


Fig. 5. Anatomical details in the aligned unbinned tomography data with a pixel length of $3.1\mu\text{m}$. Regions of interest of a selected sagittal slice in the formalin dataset showing the cerebellum (A1s), caudoputamen (A2s), and hippocampus (A3s). Zoom-ins provide cellular details in formalin (A), 100% ethanol (B), xylene (C), and paraffin (D). The density and texture of white matter (WM in A1) (A1-D1, right side) is greatly altered by embedding, while the Purkinje cell layer (arrow in A1) is clearly visible in all embeddings. The caudoputamen to fiber tract border (top arrow in A2) is especially visible in ethanol (B2), but individual cells in the somatomotor layers of the isocortex (bottom arrow in A2) are visible in all embeddings (A2-D2, upper left). Spatial resolution is approximately equal but appears poorer in paraffin (e.g. D3) because of the interpolation required to transform the data into the coordinates of formalin-fixed brain. All steps clearly capture cells of the subiculum in the retrohippocampal region (A3, arrow). All scale bars are 1 mm and the grayscale range is given by $\text{mean} \pm 2.5$ standard deviations of the intensities in the full brain mask per embedding.



(caption on next column)

Fig. 6. Enhancement of fiber tract contrast in ethanol solutions. Selected regions of interest showing fiber tracts within virtual sagittal, axial, and coronal slices are given across the entire embedding process after registration. Relative density of fiber tracts increased with respect to the surrounding tissue as ethanol concentration increased. The fiber tract contrast was almost entirely lost when embedded in paraffin. All scale bars are 1 mm and the grayscale range is given by mean \pm 1.5 standard deviations of the intensities in the full brain mask per embedding.

ethanol-immersed, and paraffin-embedded mouse brains (Töpperwien et al., 2019). Segmentation allowed for a statistical comparison of cell size, indicating that of Purkinje cells had shrinkage of 7% from formalin to ethanol and 7% from formalin to paraffin embedding, while cells in the granular layer had shrinkage of 30% from formalin to ethanol and 37% from formalin to paraffin embedding (Töpperwien et al., 2019). For reference, our results showed that for the full brain the mean volumetric strain from formalin to ethanol was 39% and to paraffin embedding was 56%. Thus, cell shrinkage is small compared to the shrinkage of larger anatomical regions, likely because tissue shrinkage is dominated by reduction of extracellular space during dehydration.

Preparation-induced changes in X-ray absorption coefficient of anatomical structures can enhance or invert contrast within the brain (see Figs. 4 to 6). We expect that the combination of datasets from selected embedding steps will provide complementary information and hence help to improve manual and automatic segmentation procedures (Stalder et al., 2014). Analysis of tissue density changes can inform the selection of a sample preparation protocol. We have emphasized the examples of ethanol solutions to highlight fiber tracts (Fig. 6) and paraffin embedding for visualizing the layers of the cerebellum (Fig. 5D1). Compared with formalin, fiber tracts in the caudoputamen showed 15-fold increase in contrast with surrounding tissue after immersion in 100% ethanol. This suggests that ethanol fixation should be used in studies of fiber orientation distribution, e.g. for validation of diffusion MRI (Trinkle et al., 2021; Foxley et al., 2021).

We postulate that the changes in volume and relative absorption coefficient of the fiber tracts can be explained by considering the distribution of water in the brain tissue. The space between the lipid bilayers that compose the myelin lamellae is filled with bound water, commonly referred to as myelin water, which can be observed with MRI systems and has significant clinical importance (Faizy et al., 2020; Birkel et al., 2021). Water in the surrounding tissue is mainly free water, which can be easily replaced by ethanol during immersion (Leist et al., 1986). The composition of myelin lipid bilayers of the central nervous system is about half cholesterol and one quarter phospholipids (Poitelon et al., 2020), the former is more soluble in xylene than ethanol and the latter more soluble in ethanol than xylene. Over the course of ascending ethanol solutions, free water is replaced by lower-absorbing ethanol, while bound water remains within myelin lipid multi-bilayer membranes and with higher relative absorption. This may also explain the increasing contrast between granular and molecular layers of the cerebellum, where the former is more cell-rich and thus contains more bound than free water. During the transition from ethanol to xylene, a greater amount of myelin lipids are dissolved, likely resulting in a breakdown of the membranes and release of the myelin water, reducing the absorption coefficient of fiber tracts relative to the surroundings. Additionally, electrostatic forces on myelin in ethanol and dissolving of lipids in xylene may lead to size changes of fibers, which could help to further explain the observed fiber tract shrinkage and X-ray absorption changes. Small angle X-ray scattering experiments could provide insight into related changes of myelin nanostructure (Georgiadis et al., 2020, 2021; Schulz et al., 2020).

5. Conclusions

We non-rigidly registered hard X-ray microtomography datasets of the same mouse brain from the formalin-fixed to paraffin-embedded

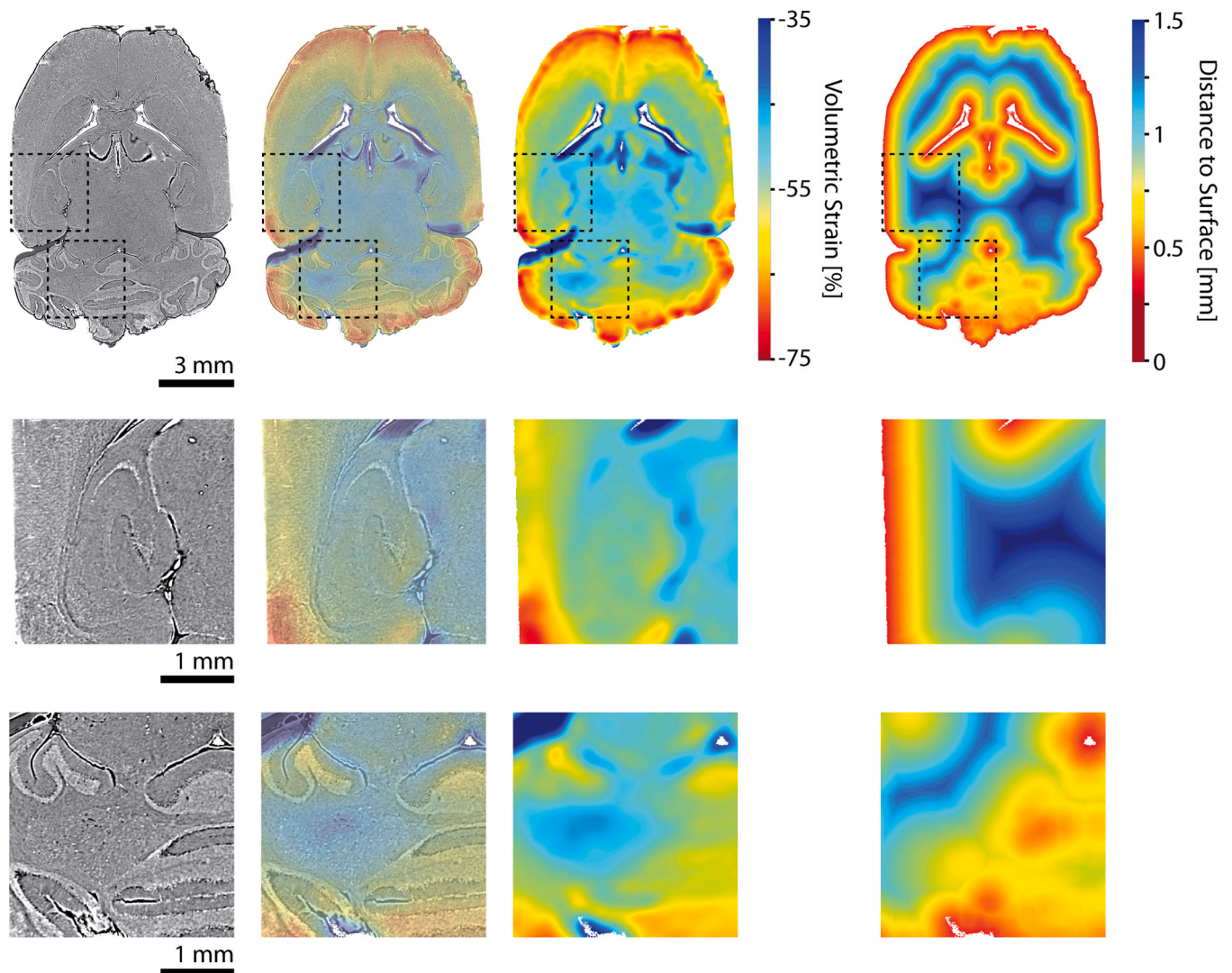


Fig. 7. Comparison of an axial slice through the paraffin embedded brain (column 1), the volumetric strain field (column 3), and the distance transform (column 4). Column 2 shows an overlay of the volumetric strain field on the tomography data. The three-dimensional distance transform was calculated from the segmentation of the paraffin embedded full brain. The grayscale range for column 1 is given by mean \pm 1.5 standard deviations of the intensities in the full brain mask.

state. Volumetric strain fields revealed local shrinkage that depended on the anatomical region and the distance to the external surface. Surprisingly, the preparation step can be selected to highlight specific anatomical features, e.g. fiber tract contrast is amplified by a factor of 15 in 100% ethanol with respect to the formalin-fixed state. The selection of optimized tissue preparation and quantification of morphology changes allows virtual histology to complement mouse brain atlases based on magnetic resonance imaging and serial histology.

CRediT author contribution statement

Griffin Rodgers: Conceptualization, Methodology, Software, Formal analysis, Investigation, Data curation, Writing – original draft, Writing – review & editing, Visualization, Funding acquisition. **Christine Tanner:** Software, Formal analysis, Investigation, Writing – review & editing, Visualization, Supervision. **Georg Schulz:** Conceptualization, Methodology, Investigation, Writing – review & editing, Supervision. **Alexandra Migga:** Validation, Formal analysis, Writing – review & editing, Visualization. **Willy Kuo:** Resources, Writing – review & editing. **Christos Bikis:** Methodology, Formal analysis, Writing – review & editing. **Mario Scheel:** Resources, Writing – review & editing. **Vartan Kurtcuoglu:** Writing – review & editing, Supervision, Project

administration, Funding acquisition. **Timm Weitkamp:** Resources, Writing – review & editing, Funding acquisition. **Bert Müller:** Conceptualization, Methodology, Investigation, Resources, Writing – review & editing, Visualization, Supervision, Project administration, Funding acquisition.

Declaration of Competing Interest

None.

Data availability

The tomographic data from all preparation steps as well as the registration parameters and final transformations are publicly available in a Zenodo repository (<https://doi.org/10.5281/zenodo.4651412>) (Rodgers et al., 2021c). Data registration and transformations can be performed with the provided parameter files and the open source software *elastix/transformix* (<https://elastix.lumc.nl/>) (Klein et al., 2010; Shamonin et al., 2014). The 3 \times downsampled volumes can be immediately downloaded. Due to the large data sizes, the full resolution data will be made available by request to the first author.

Acknowledgment

This work was carried out under Synchrotron SOLEIL experiment No. 20190424. The authors thank J. Perrin and D. Guillaume of the ANATOMIX beamline at Synchrotron SOLEIL for support during the beam time. ANATOMIX is an Equipment of Excellence (EQUIPEX) funded by the Investments for the Future program of the French National Research Agency (ANR), project NanoimagesX, grant no. ANR-11-EQPX-0031. W.K. and V.K. acknowledge support from the Swiss National Science Foundation via NCCR Kidney.CH and Project No. 153523. G.R., C. T., and B.M. acknowledge support from the Swiss National Science Foundation Project No. 185058.

References

- Albers, J., Pacilé, S., Markus, M., Wiart, M., Vande Velde, G., Tromba, G., Dullin, C., 2018. X-ray-based 3D virtual histology-adding the next dimension to histological analysis. *Mol. Imaging Biol.* 20 (5), 732–741. <https://doi.org/10.1007/s11307-018-1246-3>.
- Birkel, C., Doucette, J., Fan, M., Hernández-Torres, E., Rauscher, A., 2021. Myelin water imaging depends on white matter fiber orientation in the human brain. *Magn. Reson. Med.* 85 (4), 2221–2231. <https://doi.org/10.1002/mrm.28543>.
- C. Culling, Chapter 2: Methods of examination of tissues and cells, in: C. Culling (Ed.), *Handbook of Histopathological and Histochemical Techniques*, 3rd ed., Butterworth-Heinemann, 1974, 19–25. <https://doi.org/10.1016/B978-0-407-72901-8.50009-3>.
- Chen, F., Tillberg, P.W., Boyden, E.S., 2015. Expansion microscopy. *Science* 347 (6221), 543–548. <https://doi.org/10.1126/science.1260088>.
- Crum, W., Griffin, L., Hill, D., Hawkes, D., 2003. Zen and the art of medical image registration: correspondence, homology, and quality. *NeuroImage* 20 (3), 1425–1437. <https://doi.org/10.1016/j.neuroimage.2003.07.014>.
- Dice, L.R., 1945. Measures of the amount of ecologic association between species. *Ecology* 26 (3), 297–302. <https://doi.org/10.2307/1932409>.
- Dyer, E.L., Gray Roncal, W., Prasad, J.A., Fernandes, H.L., Gürsoy, D., De Andrade, V., Fezzaa, K., Xiao, X., Vogelstein, J.T., Jacobsen, C., Körding, K.P., Kasthuri, N., 2017. Quantifying mesoscale neuroanatomy using X-ray microtomography. *eNeuro* 4. <https://doi.org/10.1523/ENEURO.0195-17.2017>.
- Faizy, T.D., Thaler, C., Broocks, G., Flottmann, F., Leischner, H., Knipf, H., Nawabi, J., Schön, G., Stellmann, J.-P., Kemmling, A., Reddy, R., Heit, J.J., Fiehler, J., Kumar, D., Hanning, U., 2020. The myelin water fraction serves as a marker for age-related myelin alterations in the cerebral white matter – a multiparametric MRI aging study. *Front. Neurosci.* 14, 136. <https://doi.org/10.3389/fnins.2020.00136>.
- Foxley, S., Sampathkumar, V., De Andrade, V., Trinkle, S., Sorokina, A., Norwood, K., La Riviere, P., Kasthuri, N., 2021. Multi-modal imaging of a single mouse brain over five orders of magnitude of resolution. *NeuroImage* 238, 118250. <https://doi.org/10.1016/j.neuroimage.2021.118250>.
- Georgiadis, M., Schroeter, A., Gao, Z., Guizar-Sicairos, M., Novikov, D.S., Fieremans, E., Rudin, M., 2020. Retrieving neuronal orientations using 3D scanning SAXS and comparison with diffusion MRI. *NeuroImage* 204, 116214. <https://doi.org/10.1016/j.neuroimage.2019.116214>.
- Georgiadis, M., Schroeter, A., Gao, Z., Guizar-Sicairos, M., Liebi, M., Leuze, C., McNab, J. A., Balolia, A., Veraart, J., Ades-Aron, B., Kim, S., Shepherd, T., Lee, C.H., Walczak, P., Chodankar, S., DiGiacomo, P., David, G., Augath, M., Zerbi, V., Sommer, S., Rajkovic, I., Weiss, T., Bunk, O., Yang, L., Zhang, J., Novikov, D.S., Zeineh, M., Fieremans, E., Rudin, M., 2021. Nanostructure-specific X-ray tomography reveals myelin levels, integrity and axon orientations in mouse and human nervous tissue. *Nat. Commun.* 12 (1), 2941. <https://doi.org/10.1038/s41467-021-22719-7>.
- Hansen, P.C., 2000. The L-curve and its use in the numerical treatment of inverse problems. In: Johnston, P. (Ed.), *Computational Inverse Problems in Electrocardiology*. WIT Press, pp. 119–142 (*Advances in Computational Bioengineering*).
- Hardy, W.B., 1899. On the structure of cell protoplasm. *J. Physiol.* 24 (2), 158–210. <https://doi.org/10.1113/jphysiol.1899.sp000755>.
- Hieber, S.E., Bikis, C., Khimchenko, A., Schweighauser, G., Hench, J., Chicherova, N., Schulz, G., Müller, B., 2016. Tomographic brain imaging with nucleolar detail and automatic cell counting. *Sci. Rep.* 6, 32156. <https://doi.org/10.1038/srep32156>.
- Katsamenis, O.L., Olding, M., Warner, J.A., Chatelet, D.S., Jones, M.G., Sgalla, G., Smit, B., Larkin, O.J., Haig, I., Richeldi, L., Sinclair, I., Lackie, P.M., Schneider, P., 2019. X-ray micro-computed tomography for nondestructive three-dimensional (3D) X-ray histology. *Am. J. Pathol.* 189 (8), 1608–1620. <https://doi.org/10.1016/j.ajpath.2019.05.004>.
- Khimchenko, A., Deyhle, H., Schulz, G., Schweighauser, G., Hench, J., Chicherova, N., Bikis, C., Hieber, S.E., Müller, B., 2016. Extending two-dimensional histology into the third dimension through conventional micro computed tomography. *NeuroImage* 139, 26–36. <https://doi.org/10.1016/j.neuroimage.2016.06.005>.
- Khimchenko, A., Bikis, C., Pacureanu, A., Hieber, S.E., Thalman, P., Deyhle, H., Schweighauser, G., Hench, J., Frank, S., Müller-Gerbl, M., Schulz, G., Cloetens, P., Müller, B., 2018. Hard X-ray nanoholotomography: large-scale, label-free, 3D neuroimaging beyond optical limit. *Adv. Sci.* 5 (6), 1700694. <https://doi.org/10.1002/adv.201700694>.
- Klein, S., Staring, M., Murphy, K., Viergever, M.A., Pluim, J.P.W., 2010. elastix: a toolbox for intensity-based medical image registration. *IEEE Trans. Med. Imag.* 29, 196–205. <https://doi.org/10.1109/TMI.2009.2035616>.
- Kuan, A.T., Phelps, J.S., Thomas, L.A., Nguyen, T.M., Han, J., Chen, C.-L., Azevedo, A.W., Tuthill, J.C., Funke, J., Cloetens, P., Pacureanu, A., Lee, W.-C.A., 2020. Dense neuronal reconstruction through X-ray holographic nano-tomography. *Nat. Neurosci.* 23 (12), 1637–1643. <https://doi.org/10.1038/s41593-020-0704-9>.
- Leist, D.P., Nettleton, G.S., Feldhoff, R.C., 1986. Determination of lipid loss during aqueous and phase partition fixation using formalin and glutaraldehyde. *J. Histochem. Cytochem.* 34 (4), 437–441. <https://doi.org/10.1177/34.4.3081623>.
- Ma, Y., Smith, D., Hof, P., Foerster, B., Hamilton, S., Blackband, S., Yu, M., Benveniste, H., 2008. In vivo 3D digital atlas database of the adult C57BL/6J mouse brain by magnetic resonance microscopy. *Front. Neuroanat.* 2, 1. <https://doi.org/10.3389/neuro.05.001.2008>.
- Müller, B., Lang, S., Dominiotto, M., Rudin, M., Schulz, G., Deyhle, H., Germann, M., Pfeiffer, F., David, C., Weitkamp, T., 2008. High-resolution tomographic imaging of microvessels. *SPIE*, pp. 89–98.
- Pluim, J.P., Muenzing, S.E., Eppenhof, K.A., Murphy, K., 2016. The truth is hard to make: validation of medical image registration. 2016 23rd International Conference on Pattern Recognition (ICPR). IEEE, pp. 2294–2300. <https://doi.org/10.1109/ICPR.2016.7899978>.
- Poitelton, Y., Kopec, A.M., Belin, S., 2020. Myelin fat facts: an overview of lipids and fatty acid metabolism. *Cells* 9 (4). <https://doi.org/10.3390/cells9040812>.
- Quester, R., Schröder, R., 1997. The shrinkage of the human brain stem during formalin fixation and embedding in paraffin. *J. Neurosci. Methods* 75 (1), 81–89. [https://doi.org/10.1016/S0165-0270\(97\)00050-2](https://doi.org/10.1016/S0165-0270(97)00050-2).
- Rodgers, G., Kuo, W., Schulz, G., Scheel, M., Migga, A., Bikis, C., Tanner, C., Kurtcuoglu, V., Weitkamp, T., Müller, B., 2021a. Virtual histology of an entire mouse brain from formalin fixation to paraffin embedding. Part 1: data acquisition, anatomical feature segmentation, global volume and density tracking. *J. Neurosci. Methods* 364, 109354 (submitted for publication).
- Rodgers, G., Schulz, G., Kuo, W., Scheel, M., Kurtcuoglu, V., Weitkamp, T., Müller, B., Tanner, C., 2021b. Non-rigid registration to determine strain fields during mouse brain fixation and embedding. *Proc. SPIE*, pp. 55–65. <https://doi.org/10.1117/12.2583632>.
- Rodgers, G., Schulz, G., Kuo, W., Tanner, C., Müller, B., Microtomography of a mouse brain from formalin fixed to paraffin embedded: datasets and registration parameters, 2021c. <https://zenodo.org/record/4651412>.
- Schnabel, J.A., Tanner, C., Castellano-Smith, A.D., Degenhard, A., Leach, M.O., Hose, D. R., Hill, D.L., Hawkes, D.J., 2003. Validation of nonrigid image registration using finite-element methods: application to breast MR images. *IEEE Trans. Med. Imag.* 22 (2), 238–247. <https://doi.org/10.1109/TMI.2002.808367>.
- Schulz, G., Crooijmans, H.J.A., Germann, M., Scheffler, K., Müller-Gerbl, M., Müller, B., 2011. Three-dimensional strain fields in human brain resulting from formalin fixation. *J. Neurosci. Methods* 202 (1), 17–27. <https://doi.org/10.1016/j.jneumeth.2011.08.031>.
- Schulz, G., Deyhle, H., Bikis, C., Bunk, O., Müller, B., 2020. Imaging the orientation of myelin sheaths in a non-stained histology slide of human brain. *Prec. Nanomed.* 3 (4), 656–665. <https://doi.org/10.33218/001c.17211>.
- Shamonin, D., Bron, E., Lelieveldt, B., Smits, M., Klein, S., Staring, M., 2014. Fast parallel image registration on CPU and GPU for diagnostic classification of Alzheimer's disease. *Front. Neuroinform.* 7, 50. <https://doi.org/10.3389/fninf.2013.00050>.
- Stalder, A.K., Ilgenstein, B., Chicherova, N., Deyhle, H., Beckmann, F., Müller, B., Hieber, S.E., 2014. Combined use of micro computed tomography and histology to evaluate the regenerative capacity of bone grafting materials. *Int. J. Mater. Res.* 105 (7), 679–691. <https://doi.org/10.3139/146.111050>.
- Strotton, M.C., Bodey, A.J., Wanelik, K., Darrow, M.C., Medina, E., Hobbs, C., Rau, C., Bradbury, E., 2018. Optimising complementary soft tissue synchrotron X-ray microtomography for reversibly-stained central nervous system samples. *Sci. Rep.* 8, 12017. <https://doi.org/10.1038/s41598-018-30520-8>.
- Töpperwien, M., van der Meer, F., Stadelmann, C., Salditt, T., 2018. Three-dimensional virtual histology of human cerebellum by X-ray phase-contrast tomography. *Proc. Natl. Acad. Sci. U. S. A.* 115 (27), 6940–6945. <https://doi.org/10.1073/pnas.1801678115>.
- Töpperwien, M., Markus, A., Alves, F., Salditt, T., 2019. Contrast enhancement for visualizing neuronal cytoarchitecture by propagation-based X-ray phase-contrast tomography. *NeuroImage* 199, 70–80. <https://doi.org/10.1016/j.neuroimage.2019.05.043>.
- Töpperwien, M., van der Meer, F., Stadelmann, C., Salditt, T., 2020. Correlative X-ray phase-contrast tomography and histology of human brain tissue affected by Alzheimer's disease. *NeuroImage* 210, 116523. <https://doi.org/10.1016/j.neuroimage.2020.116523>.
- Trinkle, S., Foxley, S., Kasthuri, N., Rivière, P.L., 2021. Synchrotron X-ray micro-CT as a validation dataset for diffusion MRI in whole mouse brain. *Magn. Reson. Med.* 86 (2), 1067–1076. <https://doi.org/10.1002/mrm.28776>.
- Wehr, H., Bezrukov, I., Wiehr, S., Lehnhoff, M., Fuchs, K., Mannheim, J., Quintanilla-Martinez, L., Kohlhofer, U., Kneilling, M., Pichler, B., Sauter, A., 2015. Assessment of murine brain tissue shrinkage caused by different histological fixatives using magnetic resonance and computed tomography imaging. *Histol. Histopathol.* 30, 601–613. <https://doi.org/10.14670/HH-30.601>.
- Yushkevich, P.A., Piven, J., Hazlett, H.C., Smith, R.G., Ho, S., Gee, J.C., Gerig, G., 2006. User-guided 3D active contour segmentation of anatomical structures: significantly improved efficiency and reliability. *NeuroImage* 31, 1116–1128. <https://doi.org/10.1016/j.neuroimage.2006.01.015>.